Characterization of Broadband Microwave Signals Using a Photonic Lightweight Speckle Pattern Spectrometer

Mustapha A. Kassim, Shyqyri Haxha, *Senior Member*, IEEE, and Ian Flint

***Abstract*—The operating wavelength and modulation frequencies are critical components of every communication system. Here, we present a Speckle Pattern (SP) fibre-based spectrometer using a nominally fixed 852 nm laser to measure and calibrate the wavelength and modulation frequencies of the SP produced in Multimode Fibre (MMF). The laser wavelength is finely tuned within the 100 GHz range and at a resolution of 2 pm (picometers) by appropriately varying the laser injection currents. The wavelength-dependent SP is calibrated by varying the laser current over a pre-set range, and a series of wavelength-dependent speckle pattern data is recorded. The laser is tuned to the middle of the recorded wavelength range for the modulation frequency calibration, and a standard lithium niobate ($LiNbO_3$) electro-optic modulator (Mach–Zehnder Modulator) is applied. With ten metres of MMF, the incoming Radio Frequency (RF) is modulated in 5 GHz steps up to 40 GHz at a constant wavelength of 852.555 nm, and the generated SPs are stored separately for spectral processing and training. The wavelength-dependent SPs are trained using Artificial Intelligence (AI), with a reported prediction accuracy of 98.7% at 2 pm wavelength resolution. To the best of our knowledge, this is the first proof-of-concept of a high-resolution, low-cost SP Artificial Intelligence-based Spectrometer (SPAIS) that has been experimentally reported to predict the exact values of modulated frequencies from the modulated SPs.**

***Index Terms*—Convolutional neural network (CNN), microwave communications, microwave photonic, optical communications, radio Frequency (RF), radio over fibre, speckle pattern, wavelength-dependent speckle pattern.**

I. INTRODUCTION

THE increasing demand for advanced and efficient communication systems is driven by technological innovations and the necessity for high data rates. Due to the various limitations of traditional microwave communication technologies, microwave photonics has emerged as a promising technology. The implementation of Radio over Fibre (RoF) technology offers the potential to reduce the size and power consumption of radio terminals, including microwave photonics, which plays a significant role in the generation and processing of radio signals with low-phase noise, particularly in the expansion of the radio spectrum to millimetre-wave or terahertz frequencies. Additionally, microwave photonics facilitates the development of low-loss distribution circuits for RF or timing reference signals and the distribution of antenna signals for optical beamforming. Over the past few years, microwave and RF interferometry have been applied to a wide range of applications, including material characterisation [1], spatial displacement, noise, and temperature measurements [2], [3]. Hence, developing high-resolution optical spectrometers is of utmost significance to detect, quantify, and analyse RF-modulated signals across various applications. Optical spectrometers traditionally use diffraction gratings as the dispersive element, which ensures a one-to-one linear spectral-to-spatial match by diffracting the components of the spectrum of light waves to different spots on the Photodetector (PD) array [4], [5], [6]. This configuration, however, influences the resolution of the traditional grating-based spectrometer, as its resolution depends on the total number of grating lines on the rigid slab of material and the distance between the dispersive element and the PD [7]. Such spectrometers, such as the Optical Spectrum Analysers (OSA), are cumbersome in many measurement working environments that fibre telecommunication engineers encounter, such as buried cables, cramped data centres, etc. As a result, the grating-based spectrometer becomes cumbersome to attain a more excellent resolution, reducing the device's compactness for usage in remote areas; hence, a speckle pattern-based spectrometer is used.

On the other hand, a speckle pattern is a random intensity pattern created by the mutual interference of a collection of wavefronts with various phase ratios. In this case, the wavefronts combine to produce a wave whose amplitude and intensity fluctuate arbitrarily. [4], [7], and [23]. Although an optical system is frequently thought to suffer from the speckle pattern that emerges from repeated scattering and interference. However, despite being extremely complex, multiple scattering is still a reversible, linear, and repeatable process [23]. The specific speckle pattern produced by a coherent beam moving through disordered material depends on the spatial and temporal properties of the incident light field. The temporal changes of the speckle pattern can be employed, particularly as a spectrometer, in a time-invariant complex

The authors are with Electronics Engineering Department, Royal Holloway University of London, TW20 0EX Egham, U.K. Corresponding author: Shyqyri Haxha (email: shyqyri.haxha@rhul.ac.uk), kassim.mustapha.uk@gmail.com; and i_flint@hotmail.com).

medium to determine features of the incident light [23]. As the demand for optical spectrometers with ultra-high resolution and minimal losses continues to grow, there is a need for a more reliable technology that can mitigate the trade-off between the size and resolution of conventional optical spectrometers. Fortunately, using multimode fibre (MMF) as a dispersive element in spectrometer design has significantly advanced efforts to realise high-resolution and low-loss systems [3]. MMF offers several advantages over prisms or gratings, including relatively low cost, less weight, and the ability to propagate over a longer length while maintaining the desired spectral resolution. This technology has been explored in several studies [8]-[14] and is quickly becoming a popular solution for developing next-generation optical spectrometers. A typical example of an SP produced through a disordered medium such as MMF is shown in Fig. 1 below.

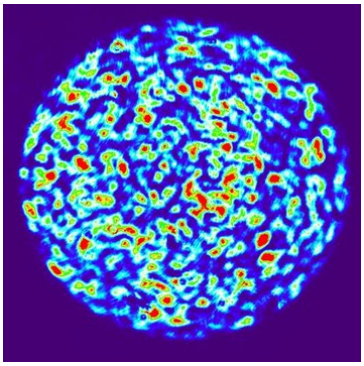

Fig. 1. SP generated from a laser source through an MMF.

In an MMF-based spectrometer, light that travels through a multimode optical fibre can take several paths, each representing a different mode. These modes create variations in the phase and amplitude of the light, resulting in interference effects causing a granular and random intensity distribution of bright and dark spots known as a speckle pattern. This speckle pattern changes over time as the optical path length of each mode fluctuates due to factors such as fibre imperfections, modal dispersion, and external disturbances. The SP arises due to the superposition of these modes when they exit the fibre after multiple reflections and refractions at the core-cladding interface [14], [15]. Such SPs have distinct features at different wavelengths of light, and these provide the required spectral-to-spatial mapping [16], [17], [18], [19]. To reconstruct the input spectrum (wavelength) from the generated SP in this configuration, the transmission matrix of the input signal is experimentally calibrated [5] with a fixed spatial polarization and profile. This reconstruction method has significant flaws, as transfer matrices on multimode fibre are susceptible to environmental perturbation and mechanical instability [20]. Therefore, complex algorithms are required to reconstruct the input spectrum from SPs in the presence of noise, as these processes are only sometimes straightforward or satisfactory [21].

Recently, artificial intelligence (AI) based algorithms (deep learning) have proven to be better at recovering the spectrum from SPs with the ability to reject noise [20]–[22]. In this research, we develop and optimise a speckled-patterned fibre-based spectrometer device using a laser with a nominally fixed wavelength of 852 nm to calibrate wavelength and modulation frequencies. We demonstrate that the wavelength and the modulation sidebands in the proposed SPs spectrometer can be determined using AI. During modulation, there is only one optical frequency at any moment. It should be noted that, from a physical perspective, it was unclear how such telecom sidebands would behave in an SP spectrometer, given the different sideband light beams that arrive at the input to the speckle interferometer at other times. The MMF's temporal dispersion will influence the speckle pattern generated by this modulation. Still, this exciting issue is not explored here since we decided to focus on the applied aspects of design.

The portability of our proposed system enables its potential for real-life application in areas such as cramped data centres and underground cables, where wavelength and frequency measurements appear challenging to achieve with conventional spectrometers. The SPs of the wavelengths or frequencies measured from these areas would then be sent to a remote station for processing.

Using deep learning, we can realise a 2 pm resolution (approximately 0.8 GHz) between two laser lines compared to the 7 pm resolution of a standard Anritsu optical spectrum analyser. Our experimental work is compared with a standard Anritsu spectrometer using a MATLAB simulation of the Anritsu resolution in a model to the results obtained from AI. As far as we know, we have developed a novel technique for AI-based RF frequency detection from modulated SPs from 10 GHz to 40 GHz, clearly showing sidebands and carrier suppression. In contrast to the existing detection methods mentioned in [36], [37], and [38], we can accurately detect the frequencies of the carrier and sidebands of modulated signals up to 40 GHz using the AI algorithm.

II. EXPERIMENTAL SET-UP & OPERATING PRINCIPLE

The experimental setup employs an 852 nm grating-stabilized, single-frequency laser diode with a narrow 15 MHz typical linewidth continuous wave (CW). The output is transmitted through a polarization-maintaining single-mode fibre of 4.5 µm core diameter, facilitated by a compact butterfly laser driver (CLD1015). The random medium utilised in this setup is a commercially available step-index multimode fibre (M15L01) with a numerical aperture of 0.22 NA and 105 µm core diameter. The connectors used in the configuration are Ferrule Connector/Angled Physical Contact (FC/APC) mating sleeves. In addition, the setup consists of a 40 GHz (LNX8540F) Intensity Mach–Zehnder Modulator (MZM) for RF modulation, an 850 ± 100 nm, 50:50 Splitter (TW850R5A1), a vector analyser (R&S ZNA67) used as the RF source, a fibre inspection scope (FS201-FC) acting as the objective lens, a 1.6 MP monochrome camera (CS165MU/M), an optical spectrum analyser (Anritsu), and a personal

computer (PC) for SP analysis. Involve.

To conduct the experiment shown in Fig. 2, the output of the laser SMF is transmitted into a 10-meter-long MMF by using a mating sleeve as a connector. The RF is switched off from the signal generator to calibrate the wavelength speckle pattern. As the light passes through the MMF, interference occurs due to the guided mode in the fibre. This phenomenon generates a distinct SP for every wavelength by sweeping the current from the laser driver. Our experiment did not involve the grating stabilisation process. The manufacturer had already performed this task as specified in the product package. The laser diode manufacturer uses Volume-Holographic-Grating-(VHG) to achieve stabilisation and houses the VHG-stabilized laser in a compact 14-pin type 1 butterfly package. This process provides a narrow-linewidth, single-frequency operation, enabling the laser to acquire 15 MHz typical linewidths. It is important to note that the laser linewidth affects the coherence length of laser light, affecting the speckle contrast. If the linewidth is highly narrowed, the speckle contrast and resolution will improve, but the susceptibility to frequency noise will increase. Therefore, balancing achieving the desired spectral resolution and managing noise levels is necessary. In this experiment, a laser with a linewidth of 15 MHz was selected based on the considerations above.

At the exit face of the MMF, the SP is focused on the camera with the aid of the objective lens. The objective lens helps to adjust the camera's focus to capture the SPs accurately. These SPs are then transferred to the PC via ThorCam, a camera control software used for scientific and industrial applications. To generate additional speckle patterns, the wavelength of the laser diode is tuned by sweeping the laser current within the stabilised region. This is done by adjusting the current in the laser diode, which causes a shift in the wavelength of the laser light. As the wavelength changes, new SPs are generated, which provides more data for analysis. For a better understanding of the process, the schematic diagram is depicted in Fig. 3. The diagram shows how the laser diode, MMF, objective lens, and camera are positioned together.

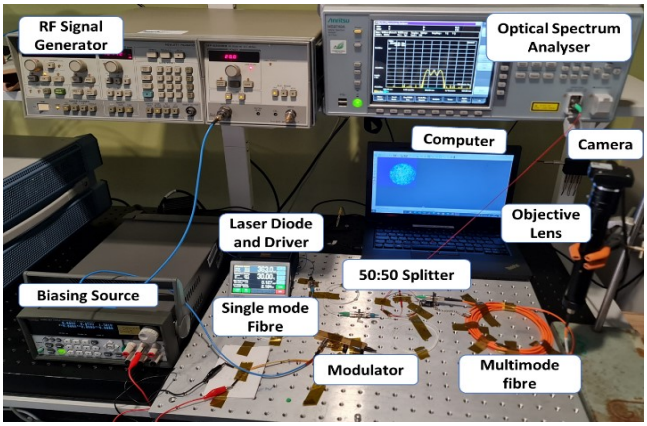

Fig. 2. Experimental setup of the proposed SP-based Spectrometer

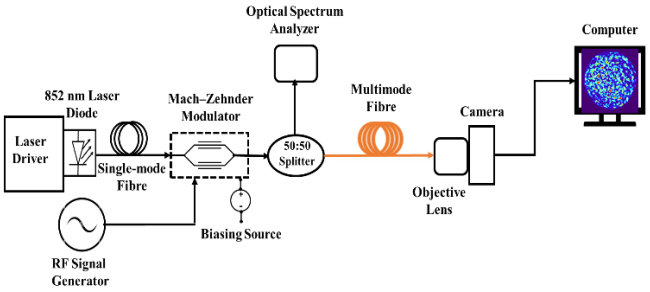

Fig. 3. Schematic diagram of the SP-based spectrometer

The intensity distribution of the SPs captured by the camera across the face of the MMF is shown using the relation in (1) below [4]:

$$\int S(\lambda)\, F(r,\lambda)\, A(\lambda) d\lambda \tag{1}$$

Where $S(\lambda)$ represents the spectral flux density of the laser, $F(r,\lambda)$ depicts the fibre's position-dependent transmission function, and $A(\lambda)$ is the camera's spectral sensitivity.

A. Wavelength Calibration

The laser injection current was varied using the laser driver over a set value to calibrate the wavelength-dependent SP. Then, a series of wavelength-dependent SP data were recorded. During the calibration, the injection current from the laser driver in Fig. 2 was varied at a step of 10 mA to record a series of wavelengths with minimum division corresponding to 0.002 nm (2 pm). This minimum shift corresponds to the minimum change with a visible de-correlation between two successive speckle patterns. These sets of wavelengths generated are plotted against their corresponding currents, and it can be observed from the graph in Fig. 4 that there are instances where some of the wavelengths hop mode after a series of steady readings. However, this is insignificant since it provides a straightforward means to change the central carrier frequency and the actual wavelength associated with a speckle pattern, which will subsequently be assigned to the various AI classes.

A change in the speckle pattern could be seen visually in real-time from the camera for a change in wavelength of 2 pm, which can also be reconstructed using AI. The resolution achieved at 2 pm can compete with most classical optical spectrometers on the market. The calibrated wavelengths are utilised as the input signal into the MMF to record the SPs. While sweeping the laser current from the laser driver, the camera is triggered to generate frames of wavelength-dependent SPs. It should be noted that the frames exhibit a minimum correlation difference of 0.002 nm. All necessary precautions, such as avoiding vibration on the measurement table and ensuring no mechanical movement of the components, were carefully preserved to obtain these results. The SP frame images are recorded over 2 minutes because of the risk that vibrations from MMF could alter the modes. A

total of 4160 SPs, corresponding to sixteen classes, are registered and stored to train the AI.

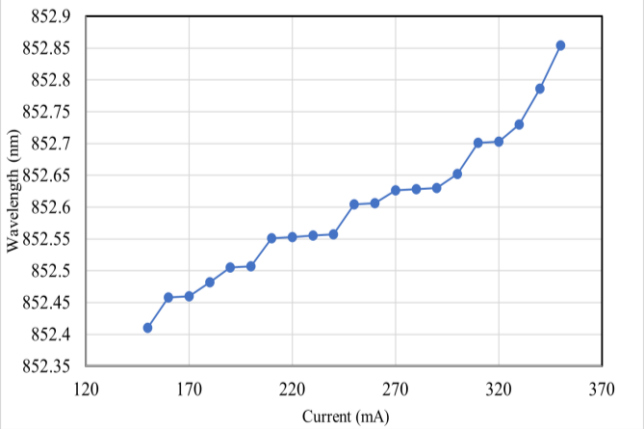

Fig. 4. Wavelength calibration of nominally fixed laser using a 10 m length of MMF

B. Speckle Pattern Modulation

The modulation speckle pattern calibration was performed using the same experimental setup shown in Fig. 2. In this scenario, the RF was turned on, and the MZM was biased from the biasing source to suppress the carrier. This makes the speckles generated by the sidebands more visible. The RF power is set at 15 dBm and made to sweep between 10 GHz and 40 GHz at a step of 5 GHz for 40 seconds at a constant carrier wavelength of 852.555 nm. A video of the SP generated at the MMF's output, captured by the camera via the microscope objective as the input RF varies from 10 GHz to 40 GHz in 5 GHz steps, is recorded. This clip demonstrates how the SPs de-correlate quickly as the RF changes, demonstrating high spectral diversity. The video is converted to frames for training and classified based on the corresponding input RF values.

The carrier wavelength is converted to carrier frequency equivalence using the following relation:

$$f_C = v/\lambda \tag{2}$$

Where f_C represents the carrier frequency, v, the velocity of light (299 792 458 m s^{-1}) and λ the carrier wavelength.

$$f_C = (2.9979\ x\ 10^8)/\ (852.555\ \text{x}\ 10^{-9})$$

$$f_C \approx 351.64\ THz$$

C. Deep Learning Spectral Reconstruction Algorithm

The uniqueness of the speckle pattern-based spectrometer lies in the algorithm used to reconstruct the input spectrum from the generated speckle pattern [23]. Unlike conventional spectral reconstruction algorithms that are sensitive to noise and thus cannot reliably recover the spectrum, the convolutional neural network has been proven to isolate noise due to its data-driven nature [24], [25]. Hence, a supervised deep learning pre-trained convolutional neural network (CNN) in MATLAB 2021a was used to reconstruct the spectrum of the generated speckle patterns.

Resnet 50 architecture (a pre-trained network) was adopted for this system configuration due to its depth of layers and reach features over a wide range of image classifications [26]. The network has an input image size of 224 by 224 pixels, a 50-layer depth of neurons, 177 layers, and an output classification of up to a thousand. This pre-trained network can avoid gradient exploding and vanishing while performing overly complex image clustering tasks [27].

Transfer Learning: The structures and the different layers of the Resnet-50 were used. However, a few modifications were made to the fully connected layer and the classification layer of the pre-trained network. The output size of the fully connected layer was modified to sixteen to match the total class required by the experiment. The weight factor and the bias learning rate were also adjusted.

Data Augmentation: sixteen classes of datasets are created, each containing 260 SPs captured at distinct wavelengths tuned by the laser current. A total of 4160 SP images were loaded on the network, and with the augmentation option, random reflection was enabled, and a 360-degree random rotation of the SP images was also enabled. The maximum horizontal rotation of the pixel was set between 0 and 1, while the random vertical translation was set between 0 and 1. The datasets are divided by the network into three categories. 70% of the data was assigned for training, 15% for validation, and 15% for testing.

Training parameters: The algorithm was trained with an initial learning rate of 10e-4, a validation frequency of fifty iterations with a mini-batch size, and a maximum epoch of 30 and 100, respectively. The stochastic gradient descent with momentum (sgdm) was selected as the solver while the training was executed in a graphics processing unit (GPU) environment.

To be able to detect the modulated frequencies, the SP frames grabbed from the sweep video explained earlier in section B above were grouped in RF steps of 5 GHz from 10 GHz to 40 GHz. A total of 200 SP frames for each class were recorded and trained. Data augmentation, a technique that modifies the initial SPs to increase the size of the training dataset artificially, was performed on the data set to guarantee a robust network.

While the training is initiated, the network automatically resizes the SPs to their input size of 224 by 224 by 3. The SPs were also batch normalised to minimise errors due to intensity fluctuations and ensure an even distribution of training data [28]–[30]. The network learns to classify the wavelength and dependent SPs with an accuracy of approximately 99%, ensuring minimal loss. With the augmented data, the trained CNN can identify the input light wavelengths with a minimal interval of 2 pm in the presence of minimal vibration and

temperature fluctuation. This is accomplished, although the conditions under which the input light is received are highly variable. This provides further evidence that a trained network (AI) can assist in developing a spectrometer that is exceptionally resistant to the effects of influences such as changes in temperature [20]. A graphical user interface also displays the frequency spectrum of the signals identified by the algorithm.

III. RESULT

A. Experimental Results

The schematic diagram in Fig. 3 illustrates the process of generating SP data, dependent on both wavelength and RF modulation. A laser beam is first pumped through an SMF with a polarization-maintained output to capture the wavelength-dependent SPs. The beam is then coupled to an MMF using a mating sleeve while the MZM is isolated. The output face of the MMF is then focused on a camera using an objective lens, which captures the SP images for viewing. The camera is connected to a PC, enabling the captured SP images to be analysed and processed. The SP generated correlates with the corresponding input wavelength. It's worth noting that the MZM modulates the RF signal applied to the device. The RF-modulation-dependent SPs are generated by varying the RF modulation frequency while keeping the wavelength constant. This process enables the SP data to be obtained under different RF modulation conditions, providing valuable information for further analysis and interpretation.

In Fig. 5 (a), a single laser line input with a wavelength of 852.505 nm was captured by the OSA. The laser input generates the SP, shown in Figure 5 (b). Similarly, Fig. 6 (a) shows a laser wavelength of 852.507 nm on the OSA. The corresponding SP for this wavelength is displayed in Figure 6(b). The reconstruction algorithm, developed to reproduce these input spectra from the speckle patterns, is discussed in the sub-discussion heading below.

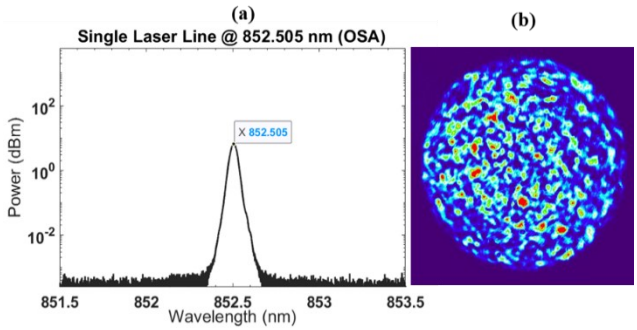

Fig. 5. (a) Wavelength of 852.505 nm as measured from Anritsu (OSA) and (b) the corresponding SP recorded at 852.505nm.

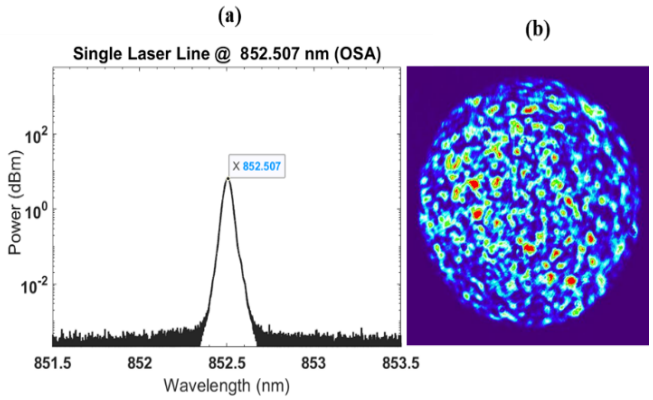

Fig. 6. (a) Wavelength of 852.507 nm as measured from Anritsu OSA and (b) the corresponding SP recorded at 852.507nm.

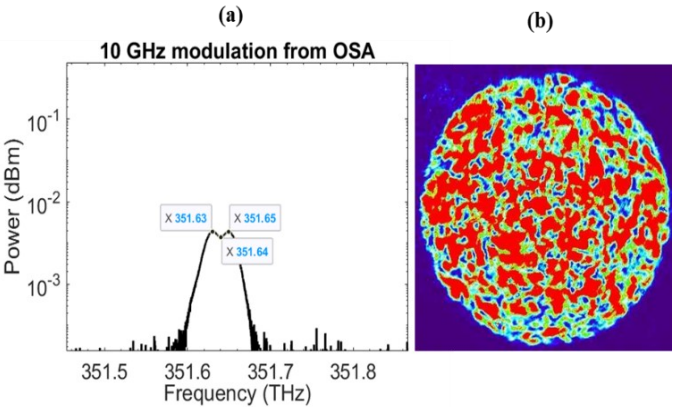

Fig. 7. (a) 10 GHz RF Modulated spectra measured by OSA and (b) the corresponding SP recorded from the modulated RF

Section II (B) above explained that SPs were generated using a modulated carrier laser RF wavelength. The RF signal was swept from 10 GHz to 40 GHz in steps of 5 GHz to obtain the desired SPs. The experimentally recorded SPs were then correlated with these RF variations, and the results are shown in Fig. 7, 8, 9, and 10. Fig. 7 (a) illustrates the experimental measurement of the modulation of 10 GHz at a constant wavelength of 852.555 nm (351.64 THz). The upper and lower sidebands of the modulated 10 GHz RF signal were recorded by the OSA at 351.65 THz and 351.63 THz, respectively. These sidebands result from the RF modulation of the carrier laser wavelength. Fig. 7 (b) shows the corresponding SP generated by the RF modulation of the carrier laser wavelength. The SP is essentially the RF signal carried by the carrier laser wavelength. The carrier laser and the RF signal combine to produce the SP that the OSA records. In other words, RF modulation of the carrier laser wavelength produces sidebands, and the resulting SPs can be correlated with the RF variations and recorded. The OSA is used to measure and record these sidebands and SPs.

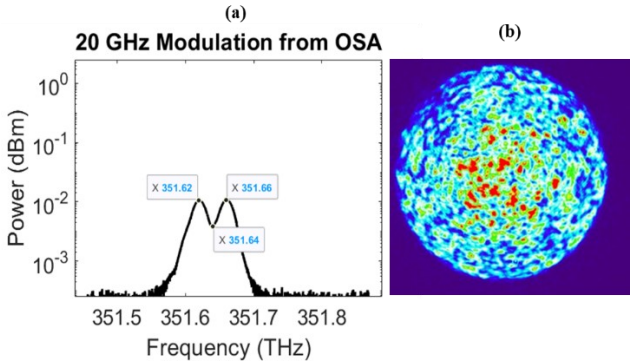

Fig. 8. (a) 20 GHz RF Modulated spectra measured by OSA and (b) the corresponding SP recorded from the modulated RF

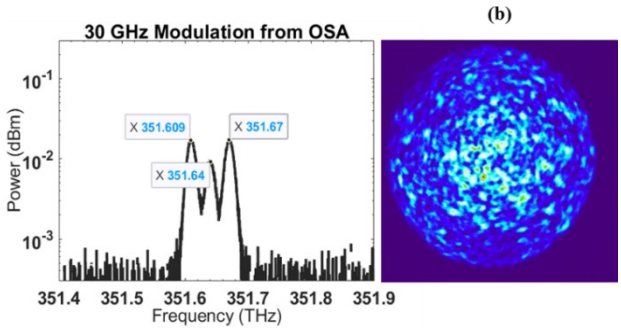

Fig. 9. (a) 30 GHz RF Modulated spectra measured by OSA and (b) the corresponding SP recorded from the modulated RF

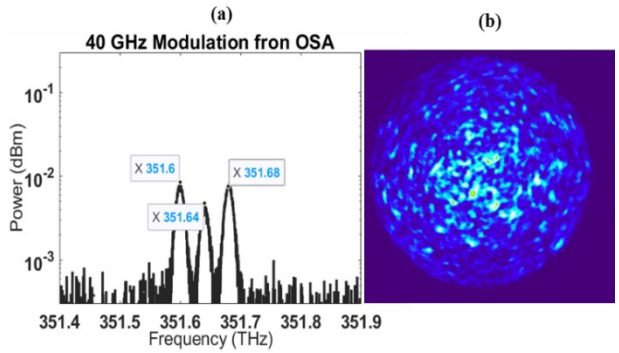

Fig. 10. (a) 40 GHz RF Modulated spectra measured by OSA and (b) the corresponding SP recorded from the modulated RF

It can also be observed that the upper and lower sidebands of the 20 GHz RF signal modulation of Fig. 8 (a) are 351.66 GHz and 351.62 GHz, respectively, while the corresponding SP is also shown in Fig. 8 (b). The same applies to Fig. 9 and 10. The recorded spectra and SPs for modulated 30 and 40 GHz are shown, respectively.

B. Simulation Results

Using the developed MATLAB Simulink, the modulation model of the Anritsu results was simulated with its limited resolution. This aided the analysis of the acquired findings by comparing the experimental simulation with the AI algorithm results.

The foundation of the modulation process relies on fundamental mathematical principles, as elucidated in the following explanation. Assuming the baseband message signal is denoted as $m(t)$, the carrier signal waveform is represented as $m_c(t)$, and A_c is the amplitude of the carrier signal. The mathematical representation of these signals can be expressed as [39].

$$m_c(t) = A_c cos\omega_c t \tag{3}$$

When the carrier signal mc(t) is multiplied by the baseband signal $m(t)$, the modulated signal $s(t)$ will have the following relationship [39]:

$$s(t) = A_c m(t) cos\omega_c t \tag{4}$$

Therefore, the parametric values used during the experiment are replicated for the simulation. These are summarised in table 1 below:

TABLE I
SIMULATION PARAMETERS

Parameters	**Values**
Carrier Frequency	351.64 THz
RF Power	18 dBm
Vπ (at null condition)	6.8 V (DC)

With the mathematical model and the parameters above, simulations of 10 GHz, 20 GHz, 30 GHz, and 40 GHz RF modulation using a carrier wavelength of 852.555 nm are performed, and the results are shown in Fig. 11 to 14 below.
The MATLAB simulation in Fig. 11 to 14 presents a smoother shape for the sideband compared to the experimental ones obtained from the OSA in Fig. 7 (a), 8 (a), 9 (a), and 10 (a). This discrepancy is due to the limited resolution of the OSA. However, despite this limitation, we could still train the AI to predict the modulated spectrum's exact frequencies accurately. It is important to note that no simulation of the Anritsu resolution was applied to Fig. 7 to 10. The Anritsu resolution refers to the minimum resolution bandwidth of the OSA, which can vary depending on the instrument's specifications. We used a resolution simulation solely for the reconstruction algorithm, which allowed us to improve the accuracy of the predictions. Overall, while the experimental data may not be as smooth as the simulation, our approach still enabled us to achieve accurate predictions of the modulated spectrum. This demonstrates the effectiveness of using AI-powered algorithms to enhance the accuracy of measurements and help more precise predictions in various fields of study.

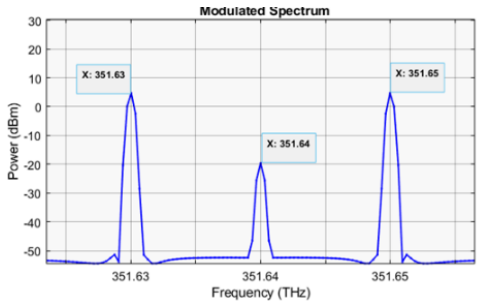

Fig. 11. Simulation result of 30 GHz of RF modulated at a carrier wavelength of 852.555nm.

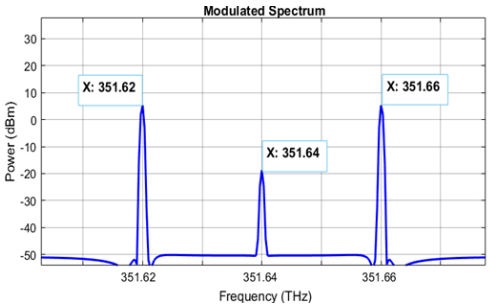

Fig. 12. Simulation result of 20 GHz of RF modulated at a carrier wavelength of 852.555nm.

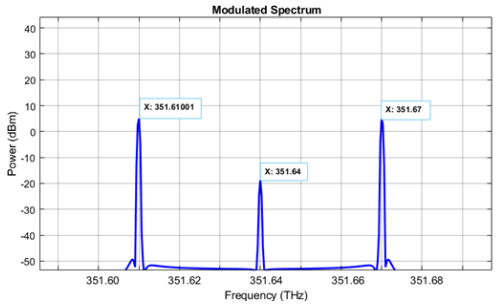

Fig. 13. Simulation result of 30 GHz of RF modulated at a carrier wavelength of 852.555nm.

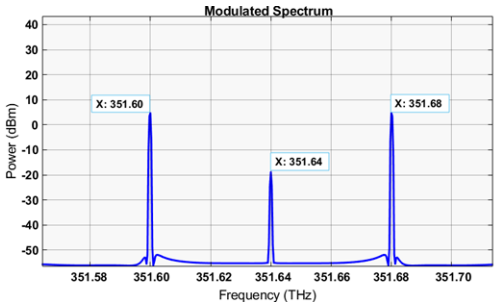

Fig. 14. Simulation result of 40 GHz of RF modulated at a carrier wavelength of 852.555nm.

C. Algorithm Results

To evaluate how well the trained network discussed in the last section works, SPs from the test sets of the dataset are loaded into the algorithm. These SPs were sampled from the test sets generated from the wavelength calibration at 852.505 nm and 852.507 nm. Fig. 16 and 17 show that the trained network can recover spectral intervals of up to 2 pm of the wavelength from the speckle pattern and this can be visualised with the developed algorithm.

Similarly, the modulated SPs generated are also trained to detect the frequency spectrum of the RF. Fig. 18 to 21 show the spectrum reconstruction of the 10 GHz, 20 GHz, 30 GHz, and 40 GHz from the modulated SPs in Fig. 7 (b), 8 (b), 9 (b), and 10 (b). Detailed explanations of the recovered spectra in Fig. 16 to 21 are provided under the discussion sub-heading.

A confusion matrix (CM) is also plotted in Fig. 15 to visualise how the CNN network classified the speckle pattern. The graph is plotted from the 15% test data, showing that 98.7% of the test data are correctly classified, as shown in the bottom right corner of the figure. From the CM, a maximum of 6.2% is required for a perfect classification of the test data per class along the diagonal of the chart. However, 3 SP images of the test data recorded at a wavelength of 852.482 nm are misclassified with those recorded at 852.630 nm, representing 0.5% test data error and 7.7% total class error. Similarly, the network misclassified 5 SP images recorded at a wavelength of 852.630 nm as 852.482 nm, representing 0.8% error of the test data in this category and 12.8% total class error. In summary, an absolute error of 1.3% resulted from the network's misclassification of some of the test data, and an overall accuracy of 98.7% was recorded by the CM (this is indicated at the bottom right corner of the CM).

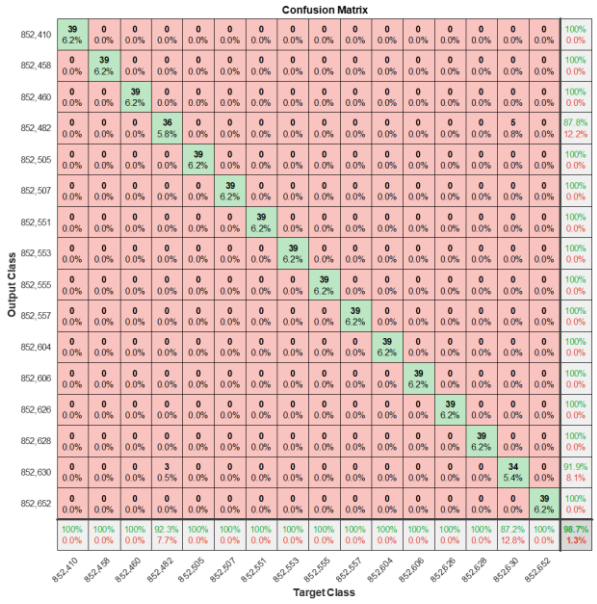

Fig. 15. Confusion matrix: Illustrating the prediction distribution from the test data.

Similarly, fig. 18 to 21 demonstrate the AI algorithm's capacity for reconstruction when experimentally generated modulated SPs are input to the network. The discussion section below goes into more detail about this.

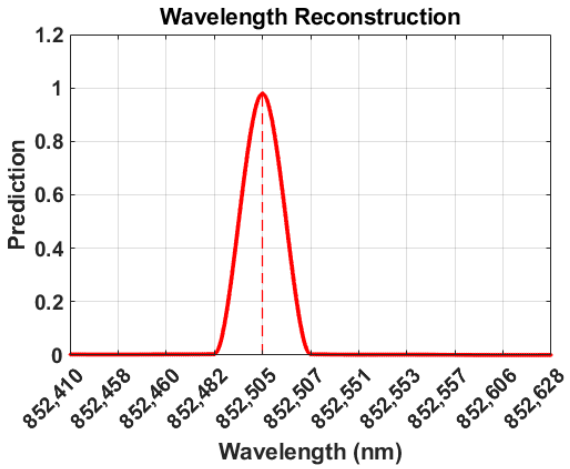

Fig. 16. A single laser line reconstruction of 852.505 nm from its SP by the convolutional neural network (AI)

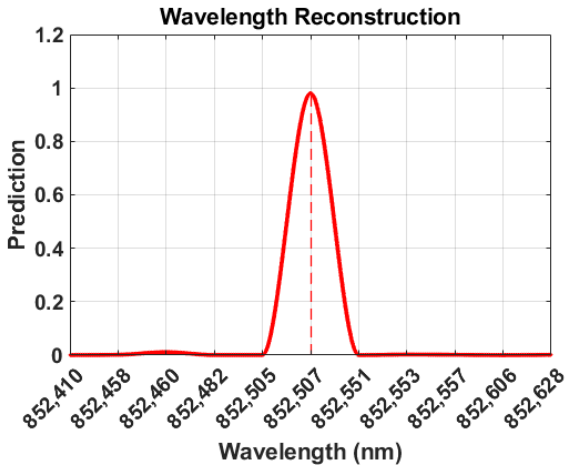

Fig. 17. A single laser line reconstruction of 852.507 nm from its SP by the convolutional neural network (AI).

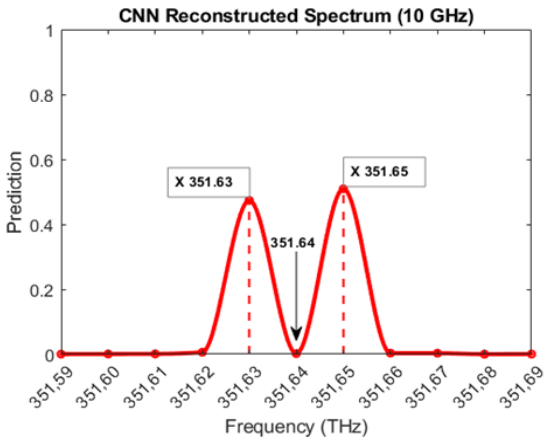

Fig. 18. AI reconstruction of the spectrum of the modulated SP at an RF of 10 GHz and a carrier frequency of 351.64 THz

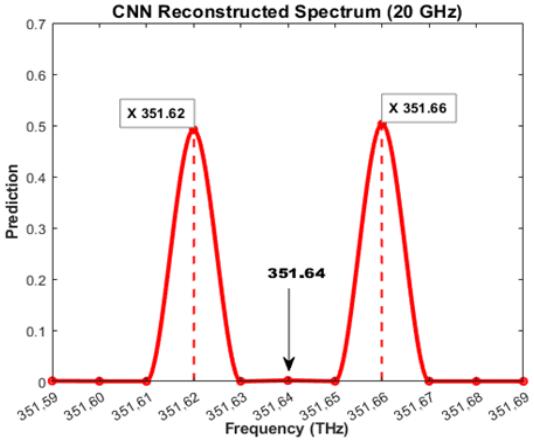

Fig. 19. AI reconstruction of the spectrum of the modulated SP at an RF of 20 GHz and a carrier frequency of 351.64 THz

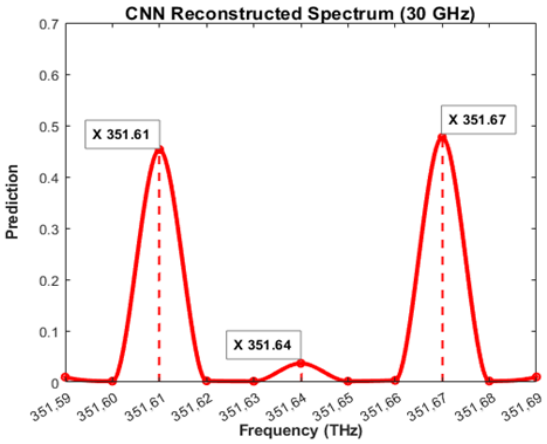

Fig. 20. AI reconstruction Spectrum of the modulated SP at an RF of 30 GHz and a carrier frequency of 351.64 THz

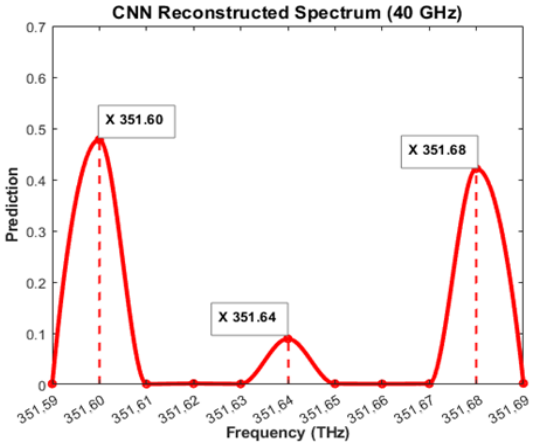

Fig. 21. AI reconstruction spectra of the modulated SP at an RF of 40 GHz and a carrier frequency of 351.64 THz

IV. DISCUSSION

Experimentally, an AI-based spectrometer (SPAIS) with a resolution of up to 2 pm and the ability to reconstruct wavelengths and modulated frequencies is presented. The research aims to create a high-resolution SP-based spectrometer using a non-tuneable laser. This spectrometer can analyse wideband RF and wavelengths (a wavemeter) from corresponding SPs.

A. Effect of Laser Diode, MMF and Camera on the Reconstruction Accuracy.

Laser Diode: The selection of a laser diode substantially impacts the speckle pattern, significantly affecting spectral reconstruction. Some of the properties of lasers that could directly influence spectral reconstruction include polarisation characteristics. The laser diode's polarisation properties can influence the light's polarisation state, potentially affecting the speckle pattern [3]. A laser diode with a linearly polarised output can be particularly useful in such cases, as it can help to reduce the variability of the speckle pattern and improve the quality and accuracy of the output. For this work, we ensure a laser with polarisation maintaining out was chosen, as mentioned in section II above. It is also essential to consider the laser linewidth as it influences the coherence length. A narrower linewidth leads to a longer coherence length, which ensures a more stable speckle. As also stated in section II above, a narrow 15 MHz Typical Linewidth (CW) was selected for this purpose.

Multimode fibre: The core size in an MMF is a crucial factor that significantly impacts the spectral reconstruction process. A larger core size allows for more spatial channels in a speckle pattern. This ultimately leads to better spectral reconstruction results. This is because the spatial channels contribute to the overall spectral response of the fibre, and an increased number of channels provides more information about the spectral components of the input signal. Maintaining a balance between achieving higher spatial channels and reduced speckle pattern resolution is also essential [3]. For this reason, we opted for step-index multimode fibre (M15L01) with a numerical aperture of 0.22 NA and 105 µm core diameter.

Camera: Similarly, camera choice significantly impacts CNN spectral reconstruction from speckle patterns as, at higher resolutions, the camera can capture more detailed information, which can help CNN learn and reconstruct spectral features more accurately. For example, higher-resolution cameras can provide more detailed information, potentially improving the CNN's ability to learn and reconstruct spectral features. The camera's frame rate becomes crucial in dynamic scenarios where the speckle patterns change rapidly, which can be particularly relevant to spectral reconstruction tasks. A higher frame rate camera can capture speckle pattern frames faster, reducing the influence of environmental factors such as vibration and temperature change. One of our goals for this project was to keep the cost of components relatively low while still achieving our design objectives. The camera employed in this experiment has a 1440 x 1080-pixel resolution (1.6 MP) sensor with 3.45 µm square pixels and a frame rate of 34.8 fps at the full sensor.

From Fig. 16 to 21 above, it can be observed that the AI successfully predicted and reconstructed the input spectra at the correct positions from the SPs generated. In Fig. 16 and 17, the AI correctly reconstructed 852.505 nm and 852.507 nm wavelengths when the SPs for these wavelengths were loaded into the network. Furthermore, the SPs in the (b) parts of Fig. 5 and 6 are captured at a resolution of 0.002 nm (2 pm) and are accurately reconstructed with the algorithm.

In Fig. 18 to 21, the algorithm also successfully predicted the carrier and the sidebands of the 10 GHz, 20 GHz, 30 GHz, and 40 GHz modulated RFs. Here, one can see that the sidebands and carriers that the AI predicted lined up at the correct frequency values, just like in the experiments in Fig. 8 to 11 and the simulation plots in Fig. 12 to 15.

Also, qualitative observations were made with the MZM in a pie (null) bias condition. The SP was even more sensitive to the RF modulation. This is unsurprising since the carrier is suppressed, and only the sideband exists. The algorithm for spectral reconstruction is designed using a convolutional neural network (RESNET 50). The pre-trained network is customised to train our dataset and intended to visualise the reconstructed spectrum graphically, as shown in Fig. 16 to 21.

The pioneering study that proposed using MMF as a dispersive element in spectrometer design is presented in [14]. This study achieved a design resolution of 0.15 nm over 25 nm bandwidth using a one-metre-long fibre and a 0.03 nm resolution over 5 nm bandwidth with a 5 m-long fibre. However, one of the drawbacks was spectra recovery from the generated SPs, as multiple algorithms had to be used to reduce the speckle noise and reconstruction errors. However, in [4], a better resolution of 8 pm of an MMF-based spectrometer was achieved. Yet, multiple algorithms, which include the transmission matrix truncated invasion technique and simulated annealing, were deployed for spectra recovery. Also, in [21], a multimode fibre 100 m long and a wavelength of 1500 nm was used to get a resolution of 1 pm at a wavelength of 1500 nm. This was done using a combination of matrix pseudo-inversion and non-linear optimisation for spectra reconstruction. In the recent advancement of this technology, a notable body of research has focused on utilising machine-learning techniques for spectral reconstruction due to their ability to denoise SPs. Notably, these studies primarily focused on reconstructing wavelengths from the generated SPs. An example of such a study is presented in [27], where a theoretical resolution of 0.1 pm is achieved. Our research aims to improve on this recent development by utilising AI to detect modulated radio frequency (RF) signals from SPs. This is different from the current detection methods, which are based on modulation classification schemes [32], [33], [34], [35] or constellation diagrams [36], [37], [38].

Furthermore, the developed AI architecture displays the reconstructed spectrum in a user-friendly graphical interface. The proposed SPAIS has a unique wavelength reconstruction resolution of 2 pm, which can be improved to sub-femtometre and attometre resolutions using a more advanced, innovative laser diode that can be finely tuned.

TABLE II
QUANTITATIVE COMPARISON OF SPECTRAL RECONSTRUCTION ALGORITHM

Aspect	Resolution	Power Density Estimation Accuracy	Computational Cost	Time/ Space Complexity	Notes
This work **(**Machine Learning Algorithm) CNN.	2 pm High, adaptive resolution	Enhanced accuracy can be achieved through adaptable data processing, effective feature extraction, generalised analysis, and pattern recognition.	Generally, machine learning models have a higher computational cost due to the requirements of model training and inference.	Relatively higher, although it depends on model complexity, size, and type of memory used for training.	The CNN algorithm requires more time and space than conventional algorithms due to its complexity and computation. Nonetheless, it is preferred in this project due to its capability to identify multiple frequencies [6] and eliminate speckle noise during training [21]. CNN can achieve an incredibly high level of resolution up to the attometre (am) scale. However, the resolution of the tuneable laser used for generating reference speckles can act as a limiting factor [6].
Non-Machine Learning Algorithm a. Truncated Inversion Technique with a Least Squares Minimization Procedure [3] b. Principal Component Analysis (PCA) [6] **c.** Sparse Optimisation [15]	**a.** 8 pm **b.** 620 pm **c.** 0.03 nm	N/A	Generally lower	Generally lower memory and time. It can significantly decrease the simulation time by employing the truncated inversion technique mentioned in (a), which can offer a reliable initial estimation [3].	On the contrary, unlike machine learning ones, conventional algorithms are relatively less expensive and have lower space complexity and computational cost, respectively. However, eliminating noise and detecting sparse signals can be challenging and require additional algorithms [3].

TABLE III
PHASE NOISE MEASUREMENT OF RF SIGNAL GENERATOR (R&SZNA67)

	Offset	100 Hz	1 kHz	10 kHz	100 kHz	200 kHz	1 MHz	5 MHz
Phase noise (meas.) in dBc (1 Hz), low phase noise mode [13]	R&S®ZNA26, R&S®ZNA43, R&S®ZNA50 and R&S®ZNA67							
	10 MHz to 100 MHz	–108	–137	–141	–139	–141	–141	–142
	100 MHz to .25 GHz	–85	–117	–125	–122	–125	–135	–142
	1.25 GHz to 2.5 GHz	–80	–111	–119	–116	–119	–130	–143
	2.5 GHz to 5 GHz	–74	–105	–113	–111	–113	–124	–139
	5 GHz to 10 GHz	–68	–99	–107	–104	–107	–118	–133
	10 GHz to 20 GHz	–62	–94	–100	–98	–101	–112	–127
	20 GHz to 26.5 GHz	–59	–91	–98	–95	–100	–103	–117
	R&S®ZNA43, R&S®ZNA50 and R&S®ZNA67							
	26.5 GHz to 40 GHz	–56	–87	–95	–90	–95	–105	–120

It is essential to state that based on the RF phase noise data in Table III above, it has been observed that the phase noise increases as the frequency of interest approaches the carrier frequency. In our situation, we converted the modal dispersion period (time delay) into frequency drifts, which in turn caused fluctuations in the wavelength of the light used. This is shown in Equation 5 below. It is important to note that the drift in RF wavelength is equivalent to the drift in phase per unit time. To put this into perspective, a time delay of 0.5 nanoseconds roughly equals a frequency of 2 GHz (2E9Hz).

If the modal dispersion period is a multimode fibre represented by $T_{d,}$ then,

$$T_d = \frac{L}{C*\eta_2} * (\eta_1 \text{^} 2) * (\eta_1 - \eta_2) \qquad (5)$$

Where L is the length of the fibre used, C is the speed of light in a vacuum, η_1 1.5 refractive index of core and η_2 1.49 refractive index of the cladding.

When L = 10 m

$$T_d = \frac{10}{3E8*1.49} * (1.5 \text{^} 2) * (1.5 - 1.49)$$

0.5 ns (6)

Considering the specification of our VNA R&SZNA67 shown in Table III above, we confirm that when the RF source is 5MHz away, it produces an output of -130dBc/Hz at 10GHz. This implies that the phase noise of the RF source is 30dB below the RF carrier frequency. The +100 comes from the conversion of 10GHz to dB. It should be noted that 5MHz converts to a time delay of 1/5MHz = 2E-7 = 200ns. Therefore, this would equate to a time delay 400 times longer than the 10m we used, i.e., 4km of fibre. Even for this length of fibre, the RF frequency drift is trivial.

As previously established, the measurement appears to be off the charts at 0.5 ns, equivalent to 2 GHz. However, the dBc/Hz remains constant at this point. This results in a value of -150dBc +100 = -50dB at a source frequency of 10GHz. At the end of the fibre, the noise power is insignificant at any given moment, even though the lens and path differences may affect the speckle on the camera. Therefore, we observe the optical frequency interference of the modulated laser, which is possible because the phase noise is so low at this 0.5ns time delay.

IV. CONCLUSION

A speckle pattern-based spectrometer based on a fixed laser diode carefully tuned to a frequency range of about 100 GHz has been designed and demonstrated experimentally. The resolution of the speckle pattern-based spectrometer is determined experimentally by the SPs decorrelation when the wavelength is adjusted by varying the laser injection current. To the best of our knowledge, this research experimentally presents proof of concept of a high-resolution 2 pm and low-cost spectrometer that can precisely measure the values of RF modulated frequencies. The incoming RF signal is modulated in 5 GHz steps up to 40 GHz using MZM, which includes a standard tuneable laser light and the Speckle Patterns (SPs) generated by the MMF, which are stored separately for spectral processing. Artificial Intelligence (AI) is used to train the wavelength-dependent produced SPs, which have a prediction accuracy of 98.7% at 2 pm wavelength resolution. In addition, we demonstrate, for the first time, a novel method for detecting modulation frequencies using Convolutional Neural Networks (CNN). The algorithm determines the carrier's exact frequency values and modulated signal sidebands.

However, a more excellent resolution can be accomplished with a longer fibre. Furthermore, the resolution of the system is also contingent upon the resolution of the laser employed for calibration. Higher resolution can also be attained at the sub-femtometre and attometre levels by this proposed work if a more advanced, cutting-edge, and finely tuneable laser diode is deployed. This research work can potentially advance the miniaturisation of bulky RF spectrometers significantly. The reported low-cost, robust, and high-resolution SP spectrometer would significantly impact advanced measurement and instrumentation in the telecommunications sector since it can deliver high-resolution RF detection and measurements and can be implemented in any robust environment. Meanwhile, future studies using AI to model and predict the power level of

modulated frequencies would be an exciting prospect, building upon the valuable insights provided by this study.

References

[1] A. Pourghorban Saghati, J. S. Batra, J. Kameoka, and K. Entesari, "A Metamaterial-Inspired Wideband Microwave Interferometry Sensor for Dielectric Spectroscopy of Liquid Chemicals," *IEEE Trans. Microw. Theory Tech.*, vol. 65, no. 7, pp. 2558–2571, Jul. 2017, doi: 10.1109/tmtt.2016.2645155.

[2] S. Kim and C. Nguyen, "A displacement measurement technique using millimeter-wave interferometry," *IEEE Trans. Microw. Theory Tech.,* vol. 51, no. 6, pp. 1724–1728, Jun. 2003, doi: 10.1109/tmtt.2003.812575.

[3] B. Redding, S. M. Popoff, and H. Cao, "All-fiber spectrometer based on speckle pattern reconstruction," *Opt. Express*, vol. 21, no. 5, p. 6584, Mar. 2013, doi: 10.1364/oe.21.006584.

[4] S. H. Kong, J. H. Correia, G. de Graaf, M. Bartek, and R. F. Wolffenbuttel, "Integrated silicon microspectrometers," IEEE Instrum. Meas. Mag., vol. 4, no. 3, pp. 34-38, Sep. 2001, doi: 10.1109/5289.953457.

[5] P. Niewczas *et al.*, "Interrogation of extrinsic Fabry-Perot interferometric sensors using arrayed waveguide grating devices," *IEEE Trans. Instrum. Meas.*, vol. 52, no. 4, pp. 1092–1096, Aug. 2003, doi: 10.1109/tim.2003.814828.

[6] Y. Wan, X. Fan, and Z. He, "Review on Speckle-Based Spectrum Analyzer," *Photonic Sensors*, vol. 11, no. 2, pp. 187–202, Mar. 2021, doi: 10.1007/s13320-021-0628-3.

[7] W. Xiong, S. Gertler, H. Yilmaz, and H. Cao, "Multimode-fiber-based single-shot full-field measurement of optical pulses," Opt. Lett., vol. 45, no. 8, p. 2462, Apr. 2020.

[8] M. J. Murray and B. Redding, "Distributed multimode fiber Φ-OTDR sensor using a high-speed camera," *OSA Continuum*, vol. 4, no. 2, p. 579, Feb. 2021, doi: 10.1364/osac.413584.

[9] A. Brientin, D. Leduc, V. Gaillard, M. Girard, and C. Lupi, "Numerical and experimental study of a multimode optical fiber sensor based on Fresnel reflection at the fiber tip for refractive index measurement," *Opt. Laser Tech*, vol. 143, p. 107315, Nov. 2021, doi: 10.1016/j.optlastec.2021.107315.

[10] N. S. Fabian, A. B. Socorro-Leranoz, I. D. Villar, S. Diaz, and I. R. Matias, "Multimode-Coreless-Multimode Fiber-Based Sensors: Theoretical and Experimental Study," *J. Lightwave Technol*, vol. 37, no. 15, pp. 3844–3850, Aug. 2019, doi: 10.1109/jlt.2019.2921609.

[11] F. Feng, W. Chen, D. Chen, W. Lin, and S.-C. Chen, "In-situ ultrasensitive label-free DNA hybridization detection using optical fibre specklegram," *Sensors and Actuators B: Chemical*, vol. 272, pp. 160–165, Nov. 2018, doi: 10.1016/j.snb.2018.05.099.

[12] Y. Sun *et al.*, "High sensitivity optical fibre strain sensor using twisted multimode fibre based on SMS structure," *Opt. Commun.*, vol. 405, pp. 416–420, Dec. 2017, doi: 10.1016/j.optcom.2017.08.059.

[13] B. Redding and H. Cao, "Using a multimode fiber as a high-resolution, low-loss spectrometer," *Opt. Lett.*, vol. 37, no. 16, p. 3384, Aug. 2012, doi: 10.1364/ol.37.003384.

[14] N. H. Wan, F. Meng, T. Schröder, R.-J. Shiue, E. H. Chen, and D. Englund, "High-resolution optical spectroscopy using multimode interference in a compact tapered fibre," *Nat. Commun*, vol. 6, no. 1, Jul. 2015, DOI: 10.1038/ncomms8762.

[15] S.F. Liew, B. Redding, M.A. Choma, H.D. Tagare, and H. Cao, "Broadband multimode fibre spectrometer," Opt. Lett., vol. 41, no. 9, pp. 2029-2032, 2016.

[16] J. Bao and M. G. Bawendi, "A colloidal quantum dot spectrometer," *Nature*, vol. 523, no. 7558, pp. 67–70, Jul. 2015, doi: 10.1038/nature14576.

[17] T. Yang *et al.*, "Miniature spectrometer based on diffraction in a dispersive hole array," *Opt. Lett.*, vol. 40, no. 13, p. 3217, Jul. 2015, doi: 10.1364/ol.40.003217.

[18] H. Cao, M. A. Choma, B. Redding, S. M. Popoff, and Y. Bromberg, "Noise analysis of spectrometers based on speckle pattern reconstruction," *Appl. Opt., Vol. 53, Issue 3, pp. 410-417*, vol. 53, no. 3, pp. 410–417, Jan. 2014, doi: 10.1364/AO.53.000410.

[19] J. Gan, M. Shen, X. Xiao, J. Nong, and F. Feng, "Deep learning enables temperature-robust spectrometer with high resolution," *Optoelectronics Letters*, vol. 17, no. 12z, pp. 705–709, Dec. 2021, doi: 10.1007/s11801-021-1126-y.

[20] B. Redding, M. Alam, M. Seifert, and H. Cao, "High-resolution and broadband all-fiber spectrometers," *Optica*, vol. 1, no. 3, p. 175, Sep. 2014, doi: 10.1364/optica.1.000175.

[21] J. Bao, D. Li, S. Li, G. Zhao, H. Sun, and Y. Zhang, "Fine-Grained Image Generation Network with Radar Range Profiles Using Cross-Modal Visual Supervision," *in IEEE Trans. Microw. Theory Tech.,* 2023.

[22] N. K. Metzger *et al.*, "Harnessing speckle for a sub-femtometre resolved broadband wavemeter and laser stabilisation," *Nat. Commun,* vol. 8, p. 15610, Jun. 2017, doi: 10.1038/ncomms15610, doi: 10.1038/ncomms15610.

[23] W. Xiong, B. Redding, S. Gertler, Y. Bromberg, H. D. Tagare, and H. Cao, "Deep learning of ultrafast pulses with a multimode fiber," *APL Photonics*, vol. 5, no. 9, p. 096106, Sep. 2020, doi: 10.1063/5.0007037.

[24] K. Xu, Z. Cai, and J. Wu, "Random pixelated grating computational spectrometer based on deep learning," *AOPC 2021: Novel Tech. & Instrum. Astron. Multi-Band Obs.*, Nov. 2021, doi: 10.1117/12.2607021

[25] K, He, X, Zhang, S, Ren, and J, Sun, "Deep residual learning for image recognition". *In Proceedings of the IEEE conference on computer vision and pattern recognition*. 2016. (pp. 770-778).

[26] L. Alzubaidi *et al.*, "Review of deep learning: concepts, CNN architectures, challenges, applications, future directions," *Journal of Big Data*, vol. 8, no. 1, Mar. 2021, Available: https://journalofbigdata.springeropen.com/articles/10.1186/s40537-021-00444-8.

[27] B. Li and D. Lima, "Facial expression recognition via ResNet-50," *Int. J. Cogn. Comput. Eng.*, vol. 2, pp. 57–64, Jun. 2021, doi: 10.1016/j.ijcce.2021.02.002.

[28] C. Garbin, X. Zhu, and O. Marques, "Dropout vs. batch normalisation: an empirical study of their impact on deep learning," *Multimedia Tools and Applications*, vol. 79, no. 19–20, pp. 12777–12815, Jan. 2020, doi: 10.1007/s11042-019-08453-9.

[29] S.-H. Choi and S. H. Jung, "Stable Acquisition of Fine-Grained Segments Using Batch Normalization and Focal Loss with L1 Regularization in U-Net Structure," *Int. J. Fuzzy Logic Intell. Syst.*, vol. 20, no. 1, pp. 59–68, Mar. 2020.

[30] S. M. Saadeh, "A New Narrowband Phase Modulation Mathematical Identity," *J. Mod. Phys.*, vol. 03, no. 06, pp. 511–515, 2012, DOI: 10.4236/jmp.2012.36069.

[31] Y. Chen, W. Shao, J. Liu, L. Yu, and Z. Qian, "Automatic Modulation Classification Scheme Based on LSTM With Random Erasing and Attention Mechanism," *IEEE Access*, vol. 8, pp. 154290–154300, 2020, doi: 10.1109/access.2020.3017641.

[32] C.-B. Ha and H.-K. Song, "Signal Detection Scheme Based on Adaptive Ensemble Deep Learning Model," *IEEE Access*, vol. 6, pp. 21342–21349, 2018, doi: 10.1109/access.2018.2825463.

[33] G. J. Mendis, J. Wei, and A. Madanayake, "Deep learning-based automated modulation classification for cognitive radio," IEEE *Int. Conf. Com. Syst. (ICCS)*, Dec. 2016.

[34] H. Ma *et al.*, "Cross Model Deep Learning Scheme for Automatic Modulation Classification," *IEEE Access*, vol. 8, pp. 78923–78931, 2020, doi: 10.1109/access.2020.2988727

[35] T. Huynh-The *et al.*, "Automatic Modulation Classification: A Deep Architecture Survey," *IEEE Access*, vol. 9, pp. 142950–142971, 2021, doi: 10.1109/access.2021.3120419.

[36] S. Peng *et al.*, "Modulation Classification Based on Signal Constellation Diagrams and Deep Learning," *IEEE Trans. Neural Netw. Learn. Syst.*, vol. 30, no. 3, pp. 718–727, Mar. 2019, doi: 10.1109/TNNLS.2018.2850703.

[37] Z. Liang, M. Tao, L. Wang, J. Su, and X. Yang, "Automatic Modulation Recognition Based on Adaptive Attention Mechanism and ResNeXt WSL Model," *IEEE Comm. Lett.*, vol. 25, no. 9, pp. 2953–2957, Sep. 2021, DOI: 10.1109/lcomm.2021.3093485.

[38] Y. Kumar, M. Sheoran, G. Jajoo, and S. K. Yadav, "Automatic Modulation Classification Based on Constellation Density Using Deep Learning," *IEEE Comm. Lett.*, vol. 24, no. 6, pp. 1275–1278, Jun. 2020, doi: 10.1109/lcomm.2020.2980840.
[39] S. A. Tretter, "Double-Sideband Suppressed-Carrier Amplitude Modulation and Coherent Detection," Springer eBooks, pp. 73–78, Jan. 1995, doi: https://doi.org/10.1007/978-1-4757-9763-3_6.

Mustapha A. Kassim completed his MSc with a distinction in the electronic engineering department at the University of Bedfordshire, United Kingdom. Before this, he also had his Higher National Diploma in Electrical and Electronic Engineering with an award of upper credit from Kaduna Polytechnic, Nigeria. He has worked as a lecturer at Kaduna Polytechnic and as a senior engineer in the ministry of power, all in Nigeria. In 2015, he received the highest national scholarship award from MSc to PhD in any institution in the world. He is in the final year of his PhD, and his research focuses on developing a high-resolution, robust, smart, and small-footprint artificial intelligence-based speckle pattern spectrometer. His research interests include speckle patterns for anti-counterfeiting and cyber security applications.

Shyqyri Haxha (Senior Member, IEEE) received the MSc and PhD degrees from City University in London in 2000 and 2004, respectively. He has also obtained several world-class industrial trainings and diplomas such as Executive MBA Cambridge Judge Business School and Mini Telecom MBAs. He was awarded the SIM Postgraduate Award from The Worshipful Company of Scientific Instrument Makers in Cambridge for his highly successful contribution in research. Currently, he is a Reader, a Director of research and Knowledge Exchange Framework (KEF) at Royal Holloway, University of London, Department of Electronic Engineering Egham, Surrey, United Kingdom. He was also a Reader in Photonics in the Computer Science and Technology, University of Bedfordshire, Luton in the United Kingdom. Prior to these posts, he was a lecturer in Optic Communication at the School of Engineering and Digital Arts, University of Kent, Canterbury, United Kingdom.
Dr. Haxha founded and leads the Microwave Photonics and Sensors (MPS) group at Royall Holloway University of London. His expertise is in designing and optimising photonic and microwave devices and systems for applications in Sensor Technology (Medical and Environmental), Nanotechnology, and Telecommunication Systems. Dr Haxha research interests are in the areas of microwave photonics, photonic crystal devices, metamaterials, photonic crystal fibers, nano-sensors, optical sensors, surface plasmon polaritons (SPP), biosensors, ultra-high-speed electro-optic modulators, compact integrated optic devices, Optical CDMA, Optical FDM, and Optical MIMO systems. He has developed and demonstrated RF over fiber transmission systems for the aviation industry, including cybersecurity protection for commercial and defense applications. He is a Chartered Engineer (CEng), Senior Member of the Institution of Electrical and Electronics Engineers (Senior MIEEE), Fellow of the Higher Education Academy (FHEA), Editorial Board Member for MDPI journals and Associate Editor of IEEE Sensors Journal. He has been a keynote speaker of numerous world class conferences.

Ian Flint received a B.Sc. degree in physics with math from the University of Reading in 1975. In 1982, he received a PhD from the same university on "The electron spin resonance of low-temperature irradiated diamond." Prof. Flint is a visiting professor at Royal Holloway University in London. He was the first to identify the role of self-interstitials in enhancing the diffusion of impurities. He is a physicist, previously working for ten years with the Universities of Reading (1978 to 1982), Hull University (from 1982 to 1983), Oxford University (1983 to 1985), and Bath University (1985 to 1989) on optoelectronics and solid-state physics. 2004, he received the BAE Systems Chairman's Gold Individual Award for a photonic microwave filter design. He is the inventor of seventeen filed patents for three different companies in the last 20 years. He is the inventor of many patent filing awards within Marconi Optical Components and Selex (Leonardo). Marconi, E2V, and BAE Systems Patents are filed in RF sampling and RF down conversion, laser hybridisation, laser machined waveguides, integrated optical isolation, micromechanical devices, blowing fibre into coil winding, monitoring surface properties, in-situ waveguide deposition, microwave photonic filters, multi-input receivers, 714 RF sampling, simulated Brillouin scattering, imaging devices and systems, etc. Authorised